JOURNAL OF GEOPHYSICAL RESEARCH, VOL. 96, SUPPLEMENT, PAGES 19,177–19,186, OCTOBER 30, 1991

Micron-Sized Particles Detected Near Neptune by the Voyager 2 Plasma Wave Instrument

D. A. GURNETT, W. S. KURTH, L. J. GRANROTH, AND S. C. ALLENDORF

Department of Physics and Astronomy, University of Iowa, Iowa City

R. L. POYNTER

Jet Propulsion Laboratory, Pasadena, California

During the Voyager 2 flyby of Neptune the plasma wave and radio astronomy instruments detected numerous impulsive signals that were interpreted as micron-sized particles striking the spacecraft. This paper presents an analysis of the particle impacts observed by the plasma wave instrument. From analysis of wideband antenna voltage waveforms a peak impact rate of 443 s^{-1} was observed near the inbound equator crossing, which occurred at a radial distance of 3.45 R_N, and a peak impact rate of 151 s^{-1} was observed near the outbound ring plane crossing, which occurred at a radial distance of 4.20 R_N. The inbound peak is offset by 146 ± 4 km north of the equatorial plane, and the outbound peak is offset by 948 ± 65 km south of the equatorial plane. A Gaussian fit of the impact rate profile has a width (to the e^{-1} points) of 537 ± 22 km for the inbound "core" component and 2,073 ± 392 km for the outbound component. These impact rates correspond to maximum number densities of a few times 10^{-3} m^{-3}. Analysis of the voltage amplitudes induced on the antenna indicates that the particles have masses ranging from 10^{-10} g to a few times 10^{-9} g, with an uncertainty of up to a factor of 10. Assuming a mass density of 1 g/cm^3, these particles would have radii in the range 5–10 μm, with an uncertainty of about a factor of 2 to 3. In addition to the high impact rates observed near the two equator crossings, an impact rate of at least 0.6 s^{-1} was observed over the entire region inside about 8 R_N, including the northern polar region. Likely sources for these particles include (1) several of the small satellites (1989N1, 1989N2, 1989N3, and 1989N4) discovered near Neptune by Voyager and (2) the rings. Electromagnetic forces may play an important role in diffusing the particles away from the equatorial plane.

1. INTRODUCTION

During the Voyager 2 flyby of Neptune, which occurred on August 25, 1989, both the plasma wave and radio astronomy instruments detected numerous impulsive events as they passed through the equatorial plane [*Gurnett et al.*, 1989; *Warwick et al.*, 1989]. This noise was similar to noise detected at the Saturn and Uranus ring plane crossings [*Scarf et al.*, 1982; *Warwick et al.*, 1982; *Aubier et al.*, 1983; *Gurnett et al.*, 1983, 1986; *Warwick et al.*, 1986; *Meyer-Vernet et al.*, 1986; *Gurnett et al.*, 1987] and is believed to be caused by micron-sized particles striking the spacecraft. As presently understood, the signal detected by the plasma wave and radio astronomy instruments is an impact ionization effect that occurs when a small dust grain hits the spacecraft at a high velocity. When a small particle strikes the spacecraft at a velocity greater than a few kilometers per second, the particle is instantly vaporized and heated to a high temperature. The resulting temperature is so high, greater than 10^5 K, that some of the vaporized material is ionized, thereby producing an expanding cloud of plasma that is detected by the electric antenna. Laboratory measurements show that the charge released is proportional to the mass of the impacting particle. Given reasonable assumptions about the charge yield and coupling efficiency to the antenna, the mass and size of the particles can be estimated from the amplitude of the voltage pulse on the antenna. The number density of the impacting particles can also be computed from the impact rate and knowledge of the spacecraft velocity and cross-sectional area.

In this paper we present a detailed analysis of the dust impacts observed by the plasma wave instrument in the vicinity of Neptune. The objectives of this paper are (1) to give a detailed description of the signals produced by the dust impacts, (2) to interpret the impact noise in terms of the number density and mass of the particles, and (3) to discuss the origin of the particles.

Paper number 91JA01270.
0148-0227/91/91JA-01270$05.00

2. OBSERVATIONS

Before discussing the observations, it is useful to review the relevant characteristics of the plasma wave instrument and the details of the Voyager 2 trajectory by Neptune. The plasma wave and radio astronomy instruments both share the same antenna. The antenna consists of two elements, each 10 m long and 1.3 cm in diameter, mounted in a V configuration. For the plasma wave instrument the antennas are operated as an electric dipole, which means that the instrument responds to the voltage difference, $V_1 - V_2$, between the two antenna elements. The radio astronomy instrument operates the antennas as two independent monopoles, which means that the instrument responds to the voltage differences between the elements and the spacecraft body. This difference in the instrument responses is important and will be considered in more detail in section 3, which discusses the interpretation of the impact signals.

The plasma wave instrument processes signals from the antennas in two ways. First, a wideband receiver is used to obtain high-resolution waveforms of the received signals

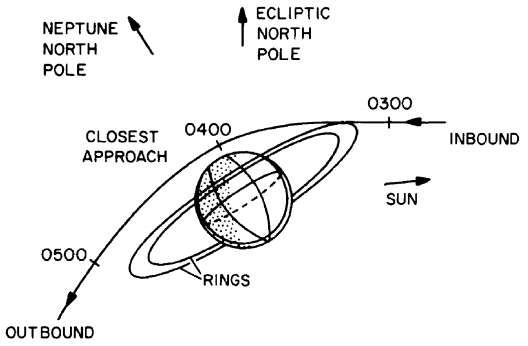

Fig. 1. A perspective view of the Voyager 2 trajectory by Neptune on August 25, 1989. The spacecraft passed through the equatorial plane twice, once on the inbound pass at about 0253 SCET and once again on the outbound pass at about 0514 SCET.

over a broad bandwidth, from 50 Hz to 12 kHz. The waveform is sampled with 4-bit resolution at a rate of 28,800 samples per second. To increase the dynamic range of the waveform measurements, an automatic gain control is used to maintain a nearly constant amplitude into the analog-to-digital converter. The time constant of the automatic gain control is 0.5 s. Second, a 16-channel spectrum analyzer is used to provide absolute measurements of the voltage spectral density over a frequency of 10 Hz to 56 kHz. The scan time of the 16-channel spectrum analyzer is 4 s, and the averaging time constant is approximately 50 ms. For a further description of the plasma wave instrument, see *Scarf and Gurnett* [1977].

The trajectory of the Voyager 2 flyby past Neptune is shown in Figure 1. The spacecraft approached Neptune from the sunward side of the planet, crossed the equatorial plane from south to north at a radial distance of 3.45 R_N (1 R_N = 24,762 km) at 0253:01.6 spacecraft event time (SCET), passed over the northern polar region at a closest approach radial distance of 1.18 R_N, and then crossed the equatorial plane from north to south at a radial distance of 4.20 R_N at 0514:52.8 SCET. Trajectory information is provided by the Jet Propulsion Laboratory. All spacecraft coordinates used in this paper are based on the ephemeris dated December 5, 1989. For a discussion of the considerations that went into the trajectory analysis and the accuracy of the navigation, see *Cesarone et al.* [1987] and *Gray* [1990]. In addition to the planet-centered radial distance coordinate it is also convenient to use a coordinate z, which is the distance from the equatorial plane to the spacecraft, measured positive in the northern hemisphere and negative in the southern hemisphere.

An overview of the dust impact noise detected by the plasma wave instrument is given in Figure 2. This illustration shows the differential antenna voltages measured by the 16-channel spectrum analyzer starting about 2 hours before the inbound equator crossing and ending about 2 hours after the outbound equator crossing. At each of the two equator crossings a well-defined burst of noise can be seen extending across nearly all of the spectrum analyzer channels. The noise intensity decreases monotonically with increasing frequency, very similar to the dust impact noise observed at Saturn and Uranus [*Scarf et al.*, 1982; *Gurnett et al.*, 1986]. The voltage spectrums at the two peaks are shown in Figure 3. In both cases the spectrum varies as f^{-4}, very similar to the spectrums obtained by the planetary radio astronomy instrument at Saturn [*Aubier et al.*, 1983] and Uranus [*Meyer-Vernet et al.*, 1986]. The root-mean-square (rms) antenna voltage, obtained at higher frequencies by integrat-

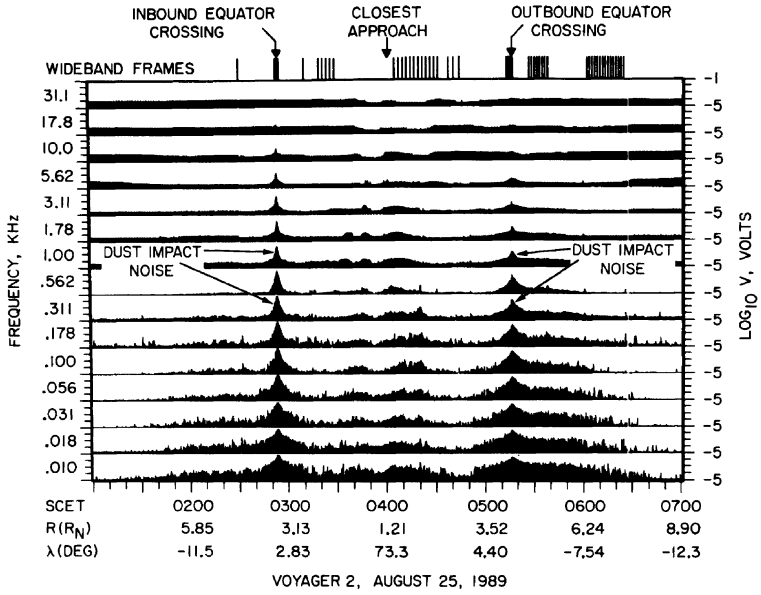

Fig. 2. The voltages measured by the 16-channel plasma wave spectrum analyzer in the vicinity of Neptune. The intense broadband peaks at the two equator crossings are caused by impacts of dust particles on the spacecraft. The much lower level spiky noise over the entire interval from 0130 to 0630 SCET is also believed to be caused by dust impacts.

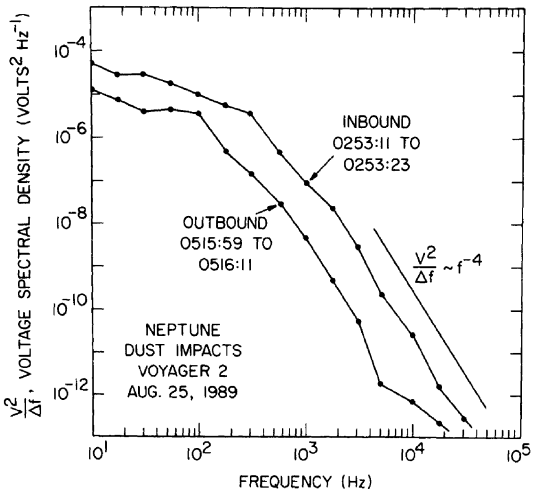

Fig. 3. The voltage spectrum of the dust impact noise near the time of maximum intensity at the two equator crossings. At frequencies above a few hundred hertz the spectrum varies as f^{-4}.

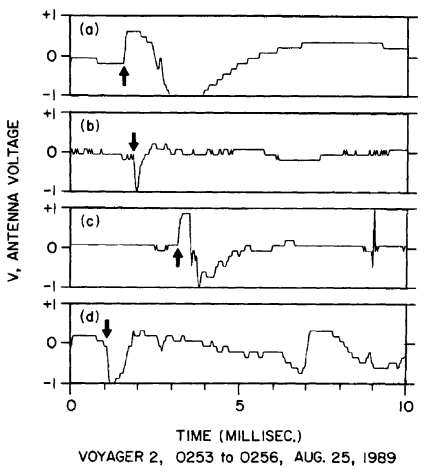

Fig. 4. Some representative dust impact waveforms from the wideband receiver in the vicinity of the inbound equator crossing. The impacts are indicated by the arrows.

ing across all of the spectrum analyzer channels, is 0.365 V for the inbound peak and 0.154 V for the outbound peak. These are the most intense signals detected by the plasma wave instrument during the Neptune flyby and are among the most intense signals ever recorded by Voyager. The peak intensity at the inbound equator crossing is slightly more intense that the dust impact noise detected at the Saturn ring plane crossing, which had a peak amplitude of 0.248 V [*Gurnett et al.*, 1983].

The best evidence that the intense noise observed near the equatorial plane is caused by dust impacts comes from the wideband receiver. Since it was anticipated that dust impacts might be observed in association with Neptune's rings, a concentration of 48-s wideband frames was scheduled near the two equator crossings. The locations of these wideband frames, along with other frames scheduled for studying plasma waves, are indicated at the top of Figure 2. The advantage of the wideband measurements is that individual impacts can be resolved in the antenna voltage waveforms, thereby leaving no doubt about the origin of the noise. Four examples of antenna voltage waveforms, selected from the wideband data obtained at the inbound equator crossing, are shown in Figure 4. These waveforms all show the characteristic signature of a particle impact, consisting of an abrupt pulse followed by a complex recovery waveform lasting from a fraction of a millisecond to several milliseconds. The rise time of the leading edge of the pulse is about 30 μs, which corresponds roughly to the rise time of the 12-kHz bandpass filter used in the wideband receiver. The pulse amplitudes vary over a wide range. Some pulses are small and well within the dynamic range of the receiver, whereas others are large and cause severe clipping. Although an automatic gain control is used in the wideband receiver, the response time of the control loop, ~0.5 s, is much too slow to adjust the gain during an individual pulse. The automatic gain control therefore only responds to the average signal amplitude. The clipped waveform that follows large pulses is caused by saturation in the receiver. If the impact waveforms from the wideband receiver are Fourier transformed and converted to a voltage spectrum, the spectrum is not as steep as the spectrum from the 16-channel spectrum analyzer. A series of wideband spectrograms selected from the inbound ring plane crossing is shown in Figure 5. As can be seen, the wideband spectrums are not as steep as the spectrums from the 16-channel spectrum analyzer. The flatter spectrums in the wideband data are almost certainly caused by the clipped square-wavelike waveforms, as in Figures 4*a* and 4*c*, which tend to give a f^{-2} spectrum. At low

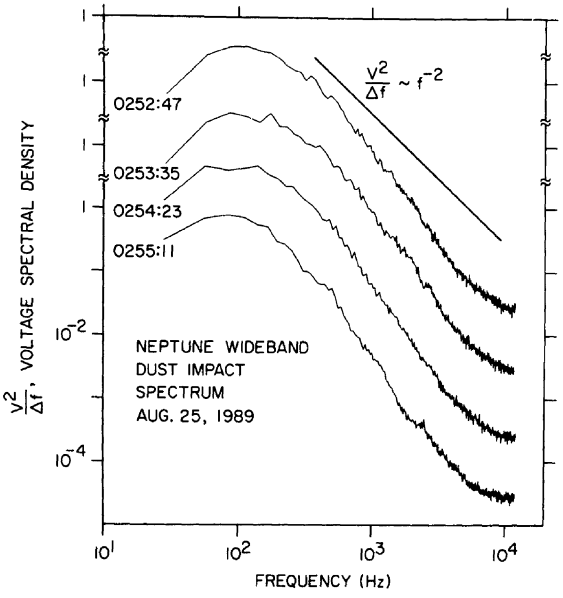

Fig. 5. Selected spectrums of dust waveforms from the wideband receiver near the inbound equator crossing. The shape of the spectrum is believed to be mainly controlled by the transient response of the wideband receiver, which often saturates (clips) following large impacts.

frequencies a well-defined maximum occurs in the spectrum, with a peak at about 100 Hz. This feature is believed to be mainly due to the recovery waveform, which is dominated by frequency components in this range.

When played through a speaker the wideband waveforms produce a sound like hail falling on a roof, similar to the dust impact sounds first discovered by *Scarf et al.* [1982] at Saturn's ring plane crossing. From visual inspection of waveforms similar to those in Figure 4 it is possible to count individual impacts, thereby giving an impact rate. Simple visual counting of pulses shows that the maximum impact rate was several hundred per second during the inbound equator crossing and about 100 impacts per second during the outbound equator crossing. To automate the counting process, a computer algorithm was developed that searches for step function changes in the antenna voltage. This algorithm was first used for analyzing dust impacts at Saturn [*Gurnett et al.*, 1983] and was used again at Uranus [*Gurnett et al.*, 1987]. Since the counting rate is sensitive to the threshold, the threshold was set during the Saturn analysis to provide good agreements with visual identification of impacts. Once adjusted, the same threshold was used for the Uranus analysis and has been used again for the Neptune analysis, thereby providing consistency among these three data sets.

Because the pulse detection algorithm would otherwise generate false events during the severely clipped recovery phase of large events, a dead time t_D is introduced in the counting algorithm after each event. The dead time is adjusted to be longer for events with larger amplitudes, since the receiver takes longer to recover after larger pulses. For large pulses the dead time can be many milliseconds. To correct for the dead time, a true counting rate R is computed from the observed counting rate R', using the standard formula for dead time corrections,

$$R = \frac{R'}{1 - \bar{t}_D R'} \tag{1}$$

where $\bar{t}_D$ is the average dead time. At the inbound equator crossing the observed impact rate was $R' = 280\ s^{-1}$, which corresponds to a corrected true impact rate of $R = 443\ s^{-1}$. The corresponding values for the outbound equator crossing are $R' = 110\ s^{-1}$ and $R = 151\ s^{-1}$.

In addition to the very high impact rates detected near the two equator crossings, evidence also exists of a lower, yet significant, impact rate over the entire region inside of about 8 R_N, including the high-latitude region near closest approach. This evidence comes from both the 16-channel spectrum analyzer data and the wideband waveform data. As can be seen in Figure 2, the low-frequency spectrum analyzer channels have a very spiky appearance over the entire region from about 0130 to 0630 SCET. Confirmation that this spiky noise is caused by impacts is provided by the numerous wideband frames that are scattered over this interval (see the top of Figure 2). Some representative waveforms from this region are shown in Figure 6. These waveforms are similar to the impact waveforms in Figure 4, except that they are often severely clipped, probably because the gain of the automatic gain control is higher in these regions of lower average signal strength. To quantify the impact rate, the average pulse rate has been determined for all of the wideband frames obtained inside 8 R_N. In some cases it was necessary to visually identify pulses in the antenna voltage waveforms, since high-frequency plasma waves sometimes produced false counts in the computer counting algorithm. These measurements show that an impact rate of at least 0.6 s^{-1} exists over the entire region inside 8 R_N.

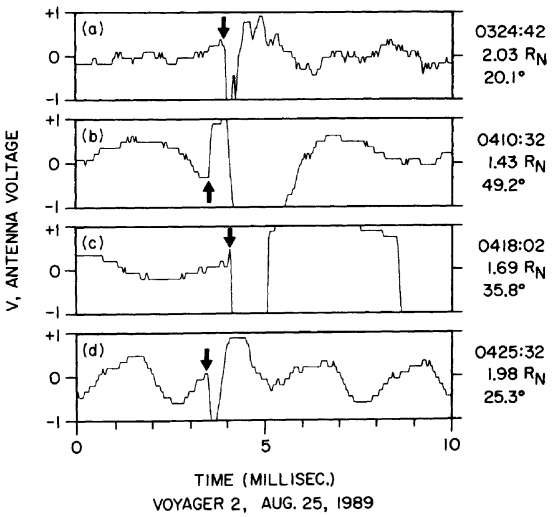

Fig. 6. Some representative dust impact waveforms in the region between the two equator crossings. A significant level of dust impacts was observed over this entire region, including the region near closest approach over the north pole (see Figure 2).

An overview of the impact rates obtained from the wideband waveform measurements is shown in Figure 7. To facilitate comparisons with the 16-channel data, this illustration has the same time scale as Figure 2. Impact rate measurements are only available where wideband frames were obtained (see the top of Figure 2), so there are

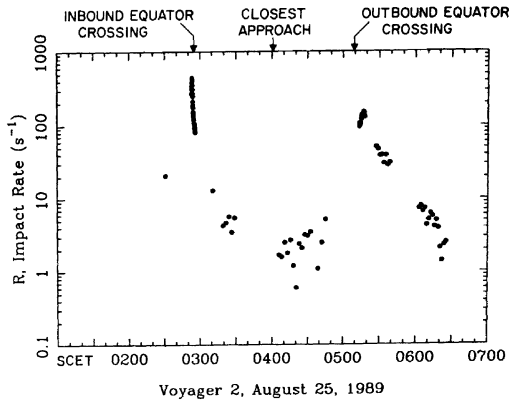

Fig. 7. The impact rate determined from the wideband waveform data plotted on a time scale comparable to Figure 2. Near the two equator crossings the impact rate was determined by a counting algorithm that includes dead time corrections. The remaining impact rates were determined by visual identification of impact waveforms. The visual impact rate determinations do not include dead time corrections because the rates are generally very low (<10 s^{-1}) and the corrections are negligible.

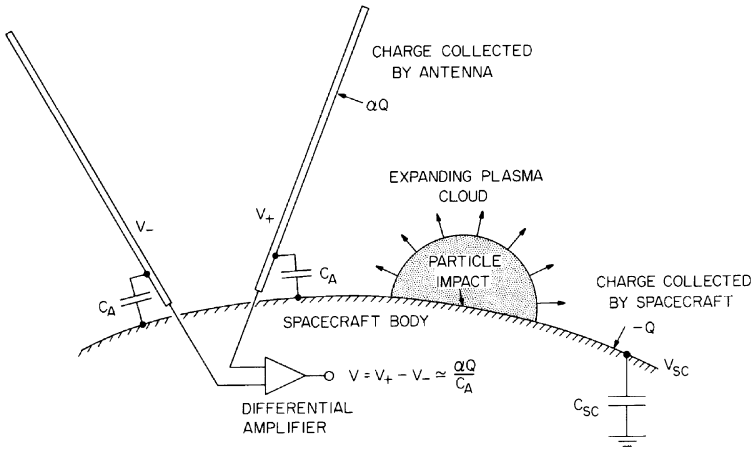

Fig. 8. The model used to analyze the voltage induced on the antenna. It is assumed that a fraction α of the charge Q released by the impact is collected by the antenna, thereby producing a voltage pulse $V = \alpha Q/C_A$, where C_A is the capacity of the antenna. The constant α serves as an effective coupling coefficient. Comparisons with the planetary radio astronomy instrument, which directly measures the charge Q emitted during an impact, indicate that $\alpha = 4.8 \times 10^{-3}$ [*Gurnett et al.*, 1987].

substantial gaps in the coverage. Figure 7 clearly shows the two sharp peaks that occur at the two ring plane crossings and the low but nonzero impact rate that exists over the entire region inside 8 R_N. Further analysis and interpretation of these data are given in section 4.

3. Coupling Mechanism

Before proceeding with a more detailed analysis it is useful to review what is known about the coupling of the dust impacts to the electric antenna. Impact ionization is now reasonably well understood. When a small particle strikes a solid surface at a high velocity, greater than a few kilometers per second, the particle, together with some of the surface material, is vaporized and heated to a high temperature, $\sim 10^5$ K [*Hornung and Drapatz*, 1981]. At this high temperature a substantial fraction of the gas is ionized, thereby producing a small plasma cloud that expands away from the impact site. The amount of ionization produced has been studied in the laboratory by several investigators. For a review of these studies, see *Grün* [1984]. The results show that to a good approximation the charge Q released is proportional to the mass m of the impacting particle,

$$Q = km \tag{2}$$

where k is a yield constant that depends on both the velocity of the particles and the composition of the particle and target. For the velocities involved in planetary flybys the yield constant varies approximately as the cube of the speed. At Saturn, where the impact velocity was 14 km/s, the average yield constant for dielectric (ice) particles striking the spacecraft was estimated by *Gurnett et al.* [1983] to be 0.21 C/g. At the Neptune equator crossings, where the impact speed for a particle in a prograde circular equatorial orbit is about 23 km/s, the corresponding yield constant is about 0.93 C/g. In the following analysis, we will use a value of $k = 1.0$ C/g for the yield constant. This value must be regarded as only a rough estimate, since uncertainties in the particle composition and other unknown factors could easily cause variations of as much as a factor of 10.

The next factor to be considered is the coupling of the emitted charge pulse to the antenna. During the Saturn ring plane crossing it was shown that the impacts are detected primarily on the spacecraft body and not on the antenna [*Gurnett et al.*, 1983]. This conclusion followed from the fact that at Saturn both positive and negative pulses occur with approximately equal occurrence rates. The occurrence of two polarities is attributed to the fact that the plasma wave instrument responds to the difference, $V_1 - V_2$, of the potentials on the two antennas. Thus an impact detected primarily by one antenna has a polarity opposite to the polarity of an impact detected by the opposite antenna. Because of the V-shaped geometry of the antenna and the details of the flyby trajectory at Saturn, the areas of the two elements projected into the direction of arrival of the impacting particles were quite different ($A_1/A_2 = 1.82$). Since the ratio of positive to negative pulses was not proportional to the projected areas of the two antennas, the impacts detected cannot be primarily on the antennas. Therefore it was concluded that the impacts must be primarily on the spacecraft body. Most likely, the polarity of the pulse is determined by the relative proximity of the impact site to the two antenna elements. Presumably, the antenna element closest to the impact site receives the largest disturbance.

Our operative model for computing the amplitude of the voltage pulse assumes that a fraction α of the emitted charge is collected by one of the antennas, thereby producing a voltage pulse of amplitude

$$V = \alpha \frac{Q}{C_A} \tag{3}$$

where C_A is the antenna capacity. A schematic model of this process is illustrated in Figure 8. Since the rise time of the pulse is very fast (microseconds), the charge collected is almost certainly due to electrons. It is easy to show that the

transit time of ions to the antenna is much slower, of the order of milliseconds. It should also be noted that it is not actually necessary that the electrons be collected by the antenna, since induced charging can also occur. Therefore it is best to think of α as simply a dimensionless coupling coefficient. The problem then is to determine α. For the plasma wave instrument this is quite difficult. The reason is that the plasma wave instrument always responds to the difference in the voltage between the two elements, which is controlled by the location of the impact site, which is not known.

Our approach to determining the coupling coefficient is to use the planetary radio astronomy (PRA) instrument to calibrate the effective response of the plasma wave (PWS) instrument to dust impacts. It turns out that the response of the PRA instrument to dust impacts is much easier to analyze, since the PRA instrument uses the antenna elements as monopoles. For a monopole the spacecraft body acts as one element of the antenna. Thus when a dust impact occurs, the charge Q is directly deposited on one of the elements, with an effective collection coefficient of unity. This model has been used by *Aubier et al.* [1983] and *Meyer-Vernet et al.* [1986] to analyze dust impacts detected by the PRA instrument. By comparing the PWS and PRA dust impact spectrums at Uranus, which overlap at about 10 kHz, *Gurnett et al.* [1987] have determined the coupling coefficient of the plasma wave instrument to be $\alpha = 4.8 \times 10^{-3}$. At present this is the best estimate we have of the effective coupling coefficient of the plasma wave instrument. In the following analysis we will use a value of $\alpha = 4.8 \times 10^{-3}$. It should be noted that the coupling coefficient represents an average over many impacts and is probably not applicable to any one impact, since the response of the antenna depends on the impact location, which is unknown.

4. Number Density and Particle Mass

Using the antenna coupling model described above, we can now proceed to estimate the number density and mass of the impacting particles. The number density, n, is given by the relation

$$R = nUA_{sc} \tag{4}$$

where R is the impact rate, U is the relative speed between the spacecraft and the particles, and A_{sc} is the effective area of the spacecraft body. The relative speed between the spacecraft and particles orbiting Neptune in circular prograde equatorial orbits is 23.6 km/s for the inbound ring plane crossing and 22.5 km/s for the outbound ring plane crossing. The effective cross-sectional area of the spacecraft has been computed by *Gurnett et al.* [1983] and is $A_{sc} = 1.66$ m^2. Measurements of the particle number density are limited to regions where wideband data are available. The impact rate, including dead time corrections, is shown in Figure 9 for the inbound equator crossing and in Figure 10 for the outbound equator crossing. In both cases a well-defined peak can be seen near the equatorial plane ($z = 0$). The inbound peak is narrower and is centered slightly north ($z > 0$) of the equator. The outbound peak is broader and is shifted substantially south ($z < 0$) of the equator. If we assume that the particle distribution depends only on the distance z from the equatorial plane, the impact rate can be

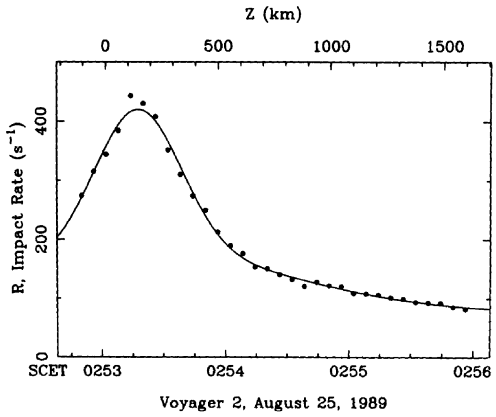

Fig. 9. The impact rate profile obtained from the wideband data near the inbound equator crossing. The solid line is the best fit to equation (5).

fit to a series of Gaussian profiles. For the inbound crossing a function of the form

$$R = R_0 + R_1 \exp\left[\frac{-(z-h)^2}{\Delta z_1^2}\right] + R_2 \exp\left[\frac{-(z-h)^2}{\Delta z_2^2}\right] \tag{5}$$

is found to give a good fit, where h is the offset of the symmetry axis from the equatorial plane and Δz is the half thickness of the respective Gaussian component. The best fit values are $R_0 = 77 \pm 7\ s^{-1}$, $R_1 = 241 \pm 11\ s^{-1}$, $R_2 = 103 \pm 7\ s^{-1}$, $h = 146 \pm 4$ km, $\Delta z_1 = 268 \pm 11$ km, and $\Delta z_2 = 921 \pm 112$ km. This fit is shown by the solid line in Figure 9. For the outbound crossing a somewhat simpler function of the form

$$R = R_0 + R_1 \exp\left[\frac{-(z-h)^2}{\Delta z_1^2}\right] \tag{6}$$

is found to give a good fit. The best fit values are $R_0 = 91 \pm 7\ s^{-1}$, $R_1 = 53 \pm 6\ s^{-1}$, $h = -948 \pm 65$ km, and $\Delta z_1 = 1036$

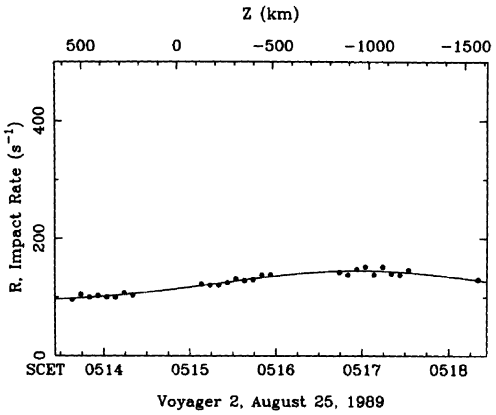

Fig. 10. The impact rate profile obtained from the wideband waveform data near the outbound equator crossing. The solid line is the best fit to equation (6).

± 196 km. This fit is shown by the solid line in Figure 10. The error limits on the parameters for the outbound crossing are not as good as for the inbound crossing because the counting rates are lower, and the wideband data coverage is not as good.

Using equation (4) with the appropriate parameters, the impact rates can be converted to number densities. The number density profiles for the inbound and outbound passes are shown in the top panels of Figures 11 and 12. The impact rate is given by the scale on the left of the panel, and the corresponding number density is shown by the scale on the right. For the inbound crossing the maximum number density is slightly greater than 10^{-2} particles per cubic meter, and for the outbound crossing the maximum number density is a few times 10^{-3} particles per cubic meter. These number densities correspond to average interparticle distances of the order of a few meters. The number densities should be quite accurate, since there is very little uncertainty in any of the quantities involved. The statistical error in the counting rate is only a few percent, and the spacecraft speed relative to the particles is known to within a fraction of a percent. Probably the largest uncertainty is in the estimate of the effective area of the spacecraft. The effective area is difficult to determine because of the complex geometries involved and because certain materials, such as plastics, have very low yield coefficients. For example, the effective area does not include the large high-gain antenna. The back side of this antenna, which is exposed to the dust impacts, is constructed of a composite material, which has a very low yield coefficient compared to other metal surfaces on the spacecraft. For a survey of the yield coefficient and effective area of various parts of the spacecraft, see *Gurnett et al.* [1983]. Considering

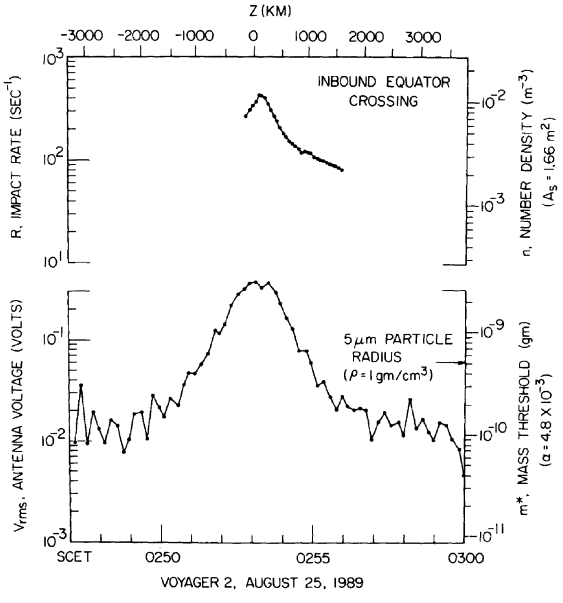

Fig. 11. A comparison of the impact rate, R, from the wideband receiver, and the rms antenna voltage, V_{rms}, from the 16-channel analyzer for the inbound equator crossing. The impact rate gives the particle number density, n, shown by the scale on the right of the top panel, and the rms antenna voltage gives the counting threshold, m^*, shown by the scale on the right of the bottom panel.

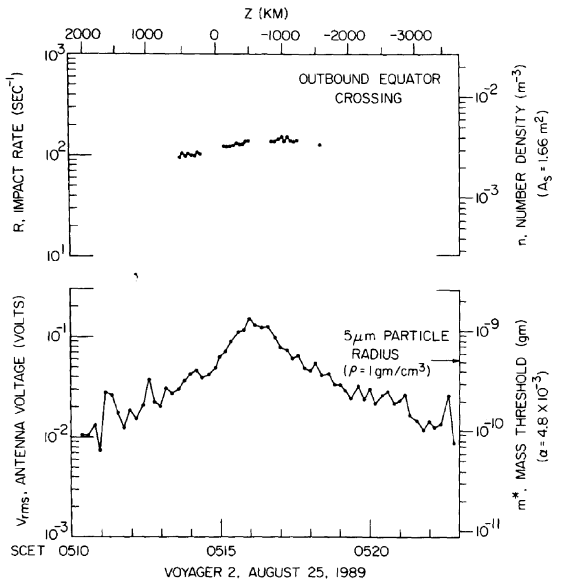

Fig. 12. A comparison of the impact rate, R, and the rms antenna voltage, V_{rms}, for the outbound equator crossing. This illustration, together with Figure 11, shows that the plasma wave instrument was detecting particles with radii of the order of 5–10 μm near two equator crossings. The number densities were of the order of a few times 10^{-3} m^{-3}.

all of these effects, we estimate that the effective area is probably accurate to within ±10–20%, which means that the number density has a comparable uncertainty.

Since the counting rate has an amplitude threshold, below which no particles are detected, it is important to estimate this threshold in terms of the mass of the particles being detected. The particle mass can be related to the amplitude of the voltage pulse on the antenna by combining equations (2) and (3), which gives

$$m = \left(\frac{C_A}{\alpha k}\right) V. \tag{7}$$

Since the automatic gain control in the wideband receiver continuously adjusts the gain to maintain a constant rms output voltage, the threshold voltage, V^*, for detecting an impact is directly proportional to the rms antenna voltage V_{rms},

$$V^* = \beta V_{rms}. \tag{8}$$

The proportionality constant β has been previously evaluated by *Gurnett et al.* [1983] and is approximately $\beta = 0.51$. Combining equations (7) and (8) gives the following mass threshold for counting impacts:

$$m^* = \left(\frac{\beta C_A}{\alpha k}\right) V_{rms}. \tag{9}$$

Using the nominal parameters ($\beta = 0.51$, $C_A = 90$ pF, $\alpha = 4.8 \times 10^{-3}$, and $k = 1.0$ C/g), the proportionality factor $\beta C_A/\alpha k$ works out to be 9.6×10^{-9} g/V. The rms antenna voltage for the inbound and outbound equator crossings,

computed by integrating the spectrum from the 16-channel spectrum analyzer, is shown in the bottom panels of Figures 11 and 12. The rms voltage, V_{rms}, is given by the scale on the left of the panel, and the corresponding mass counting threshold, m^*, using equation (9), is given by the scale on the right. Note that the mass threshold for counting impacts varies substantially during the pass. This is because the gain of the wideband receiver varies inversely with the rms voltage of the signal on the antenna. At the inbound equator crossing the threshold for detecting impacts varied from about 10^{-10} g to about 3.5×10^{-9} g. At the peak the number density, $n_{max} = 1.1 \times 10^{-2}$ m^{-3}, includes only particles with masses greater than $m^* = 3.5 \times 10^{-9}$ g. For a mass density of 1 g cm^{-3}, which is representative of a typical dielectric particle (ice, for example), the corresponding radius is 9.4 μm. More dense particles, such as silicates, would have somewhat smaller radii, and less dense, fluffy particles, would have somewhat larger radii. Similar results also apply to the outbound equator crossing. Based on these estimates it appears that the plasma wave instrument is mainly counting particles with radii of 5–10 μm and larger. Note that although the parameters α and k are quite uncertain, the particle size varies only as the cube root of these parameters, which reduces the uncertainty in the particle size, probably to within a factor of 2 or 3.

A somewhat different approach to the mass and size analysis can be obtained from the rms signal strength. As a simple model we assume that the waveforms consist of rectangular pulses of amplitude V_n and duration τ_n. Using equation (7), the rms antenna voltage averaged over time T can be written

$$V_{rms}^2 = \frac{1}{T} \sum_n V_n^2 \tau_n = \left(\frac{\alpha k}{C_A}\right)^2 \frac{1}{T} \sum m_n^2 \tau_n. \qquad (10)$$

Although the duration of the pulses varies somewhat, these variations are most likely small compared to the amplitude variations. Therefore the pulse durations are taken to be a constant $\tau_n = \tau$. The averaging time T can also be reexpressed in terms of the total number of impacts N, using the relation $N = RT$, so that

$$V_{rms}^2 = \left(\frac{\alpha k}{C_A}\right)^2 R\tau \left[\frac{1}{N} \sum m_n^2\right]. \qquad (11)$$

The quantity in the brackets is just the square of the rms mass. The rms mass is therefore directly related to the rms antenna voltage and is given by

$$m_{rms} = \left(\frac{C_A}{\alpha k}\right) \frac{1}{(R\tau)^{1/2}} V_{rms}. \qquad (12)$$

The difficulty with using this equation is that the impact rate R includes particles of all masses. Since the measured impact rate only counts particles with masses greater than m^*, if the measured impact rate is used for R, equation (12) only gives an upper limit to the rms mass. Using $\tau = 1$ ms, $R = 443$ s^{-1}, and the nominal values for the remaining parameters, the upper limit to the rms mass at the time of maximum impact rate during the inbound equator crossing works out to be $m_{rms}(\text{Max}) = 1.0 \times 10^{-8}$ g. For a particle with a density of 1 g cm^{-3} the corresponding particle radius is 13.4 μm.

From a comparison of the top and bottom panels of Figures 11 and 12 it can be seen that the impact rate and rms antenna voltage profiles are not identical. In particular, the fluctuations in the antenna voltage are larger than the fluctuations in the impact rate, and the impact rate profile does not have the same shape as the rms antenna voltage profile. Note, for example, that on the outbound pass the peaks in the impact rate and rms antenna voltage do not even occur at the same place. The difference in the fluctuation level is believed to be simply a matter of statistics. Since the sample rate of the wideband data (28,800 samples/s) is much higher than the sample rate of the 16-channel spectrum analyzer (4 samples/s), statistical fluctuations in the impact rate are expected to be much smaller than the statistical fluctuations in the rms antenna voltage. The differences in the shapes of the profile are more difficult to explain. Most likely, the differences are related to changes in the size distribution of the particles. As discussed by *Gurnett et al.* [1983], the impact rate and rms antenna voltage respond to fundamentally different quantities. The impact rate is essentially a measure of the zeroth moment of the mass distribution, integrated above the counting threshold ($m > m^*$), whereas the rms antenna voltage is determined by the second moment of the mass distribution. Although these two quantities contain information on the mass and size distribution, we have not attempted to carry out a detailed interpretation. Estimates of the mass distribution are complicated by the fact that one must somehow take into account variations in the pulse height due to changes in the impact location on the spacecraft, which is extremely difficult to analyze.

5. Discussion

Our analysis shows that the particle impacts detected by the Voyager 2 plasma wave instrument at Neptune were caused by particles with radii of the order of 10 μm and larger. The mass threshold for detecting these particles varies from about 10^{-10} g to a few times 10^{-9} g, with an uncertainty of up to a factor of 10. The particle impacts were strongly concentrated near the equatorial plane. At the inbound equator crossing the maximum number density was about 10^{-2} m^{-3}, and at the outbound equator crossing the maximum number density was a few times 10^{-3} m^{-3}. These number densities are known with good accuracy, probably to within 10–20%. A much lower level of particle impacts, corresponding to number densities of the order of 10^{-4}–10^{-6} m^{-3}, was observed over the entire pass inside about 8 R_N, including the region near closest approach over the northern polar region. The basic picture that emerges from these observations is that the dust particles are concentrated in a dense "disk" near the equatorial plane, with a broad "halo" of particles extending far from the equatorial plane. A schematic model illustrating these results is shown in Figure 13.

Although the basic model presented in Figure 13 is generally consistent with the data and is similar to the distribution of small micron-sized ring-plane particles found at other planets, there are several unique new features. For the first time at Neptune a trajectory is available that passes through the bulk of the particles on opposite sides of the planet at comparable but slightly different radial distances (see Figure 1). The resulting impact rate profiles at these two crossings show dramatic differences. Most striking is the fact that the

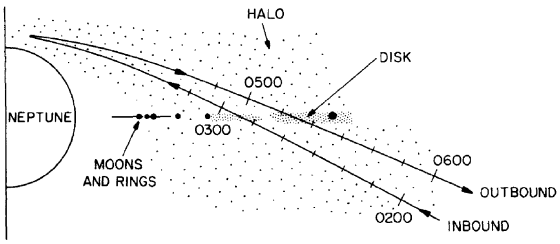

Fig. 13. The dust impacts detected by the plasma wave instruments consist of two components, a dense "disk" oriented along the equatorial plane and broad "halo" extending far from the equatorial plane. These particles probably originate from micrometeorite impacts on the numerous moons and ring particles that orbit Neptune near the equatorial plane.

inbound profile is shifted north of the equatorial plane by 146 ± 4 km, whereas the outbound profile is shifted south of the equatorial plane by 948 ± 65 km. The first-order impression is that these shifts indicate that the "disk" is tilted with respect to the equatorial plane. The corresponding tilt angle is about 0.4°. Whether this "tilt" is real and can be accounted for by gravitational perturbations such as from the large moon, Triton, or by some other effect has not been determined. It does not appear that these shifts could be caused by errors in the spacecraft ephemeris. Although a tilt or warping of the dusk disk provides the simplest interpretation, it is also possible that the shifts could be due to radial or azimuthal variations. In fact, the large differences in the maximum counting rates and the differences in the north-south thicknesses of the Gaussian fits for the inbound and outbound equator crossings shows that there are substantial radial or azimuthal variations. Without more data it is impossible to separate these functional dependences. Further work is needed to resolve these various possible interpretations.

Next we consider the origin of the particles. In other similar ring systems at Jupiter, Saturn, and Uranus, it has been shown by *Burns et al.* [1980, 1984, 1986], *Morfill et al.* [1980*a*, *b*], and others that small micron-sized particles are quickly destroyed on time scales of a few million years. The primary destruction mechanisms are shattering by collisions and sputtering by magnetospheric ions. Similar processes are almost certainly operative at Neptune. Since the particles are quickly destroyed, a suitable source must exist to produce the particles. Small micron-sized ring particles are believed to be produced by micrometeorite bombardment of satellites and large ring particles. The Voyager imaging observations show that several small satellites (1989N1, 1989N2, 1989N3, and 1989N4) and rings occur near and inside the region where Voyager crossed the equatorial plane [*Stone and Miner*, 1989]. The locations of these satellites and rings are shown in Figure 13. These objects all provide suitable sources for micron-sized particles orbiting near the equatorial plane. However, they cannot readily account for the "halo" particles observed far from the equatorial plane. Large energies are required to inject particles into orbits that are highly inclined with respect to the equatorial plane. The most likely mechanism for achieving such highly inclined orbits from a source near the equatorial plane is via electromagnetic interactions with the magnetic field of the planet. Electromagnetic interactions arise because small dust particles are charged by photoemission and electron collection from the plasma. It is easily shown that particles in the micron size range are susceptible to electromagnetic forces [*Northrop and Hill*, 1983; *Schaffer and Burns*, 1987]. The tilted magnetic field of Neptune [*Ness et al.*, 1989] also may play an important role in the electromagnetic interactions by providing an out-of-equatorial-plane force that can change the orbital inclination of the particles. Further study is required to establish the origin and dynamics of the "halo" particles.

Finally, we should make some comments on the possibility of detecting the disk particles by other means, most notably either by imaging measurements or by their effect on energetic radiation belt particles. A rough evaluation of both of these possibilities can be obtained by computing the number of particles in a column passing perpendicularly through the ring plane. Using the best fit Gaussian density profiles, the columnar number density perpendicular to the equatorial plane for the inbound equator crossing is $\pi(n_1\Delta z_1 + n_2\Delta z_2) = 1.2 \times 10^4$ particles/m^2, where n_1 and n_2 are the number densities corresponding to the counting rate terms R_1 and R_2 in equation (5). In this estimate we have ignored the constant term R_0, since this term is small and we have no way of determining the corresponding thickness. Having determined the columnar number density, we can then estimate the geometric opacity, which is the fraction of the area obscured by particles along the column. If we assume that the particles all have a radius of $r_0 = 10$ μm, which is probably an overestimate, the cross-sectional area per particle is then $A_0 = 3.1 \times 10^{-10}$ m^2. The geometric opacity is then $\tau = \pi A_0(n_1\Delta z_1 + n_2\Delta z_2) = 3.8 \times 10^{-6}$. The corresponding opacity for the outbound equator crossing is $\tau = 2.5 \times 10^{-6}$. These are extremely small opacities. Given the extremely low light intensities present at Neptune, it is exceedingly unlikely that these particles could be seen by the Voyager imaging system. In fact, no ring observations have been reported by the imaging team in the region where Voyager crossed the equatorial plane. For the absorption of energetic particles the relevant quantity is the columnar mass density. If the average mass of the particle is $m_0 = 10^{-8}$ g, then the columnar mass density is 1.2×10^{-4} g/m^2 for the inbound crossing and 7.9×10^{-5} g/m^2 for the outbound crossing. These are also very small quantities. Whether these mass densities are large enough to produce observable effects on radiation belt charged particle fluxes remains to be determined.

Acknowledgments. The authors would like to thank Ellis Miner and Bob Cesarone of the Jet Propulsion Laboratory for providing information on the navigational accuracy and trajectory determination. We also wish to thank Janice Cook-Granroth and Bruce Waggoner for their efforts in visually counting impact rates in the wideband frames. The research at the University of Iowa was supported by contract 957723 with the Jet Propulsion Laboratory.

The Editor thanks D. R. Evans and another referee for their assistance in evaluating this paper.

REFERENCES

Aubier, M. G., N. Meyer-Vernet, and B. M. Pedersen, Shot noise from grain and particle impacts in Saturn's ring plane, *Geophys. Res. Lett.*, *10*, 5, 1983.

Burns, J. A., M. R. Showalter, J. N. Cuzzi, and J. B. Pollock, Physical processes in Jupiter's ring: Clues to its origin by Jove!, *Icarus*, *44*, 339, 1980.

Burns, J. A., M. R. Showalter, and G. E. Morfill, The ethereal rings of Jupiter and Saturn, in *Planetary Rings*, edited by R. Greenbery and A. Brahic, pp. 200–272, University of Arizona Press, Tucson, 1984.

Burns, J. A., L. E. Schaffer, J. N. Cuzzi, and D. A. Gurnett, Dust in the Uranian system: Its origin and fate, *Bull. Am. Astron. Soc.*, *18*, 770, 1986.

Cesarone, R. J., K. Francis, W. J. Kosmann, S. E. Matousek, C. L. Potts, and R. W. Ridenour, Mission design challenges posed by the Voyager 2 Neptune encounter, AAA/AIAA Astrodynamics Specialist Conference Proceedings, *Pap. 87-489*, Am. Astron. Soc./Am. Inst. of Aeron. and Astronaut., Kalispell, Mo., Aug. 10–13, 1987.

Gray, D. L., S. E. Matousek, K. Francis, C. L. Potts, and R. J. Cesarone, Voyager 2 Neptune navigation results, paper presented at AIAA/AAS Astrodynamics Conference, Am. Astron. Soc./ Am. Inst. of Aeron. and Astronaut., Portland, Oreg., Aug. 20–22, 1990.

Grün, E., Impact ionization from gold, aluminum, and PCB-Z, The Giotto spacecraft impact induced plasma environment, *Eur. Space Agency Spec. Publ.*, *SP-224*, 39, 1984.

Gurnett, D. A., E. Grün, D. Gallagher, W. S. Kurth, and F. L. Scarf, Micron-sized particles detected near Saturn by the Voyager plasma wave instrument, *Icarus*, *53*, 236, 1983.

Gurnett, D. A., W. S. Kurth, F. L. Scarf, and R. L. Poynter, First plasma wave observations at Uranus, *Science*, *233*, 106, 1986.

Gurnett, D. A., W. S. Kurth, F. L. Scarf, J. A. Burns, J. N. Cuzzi, and E. Grün, Micron-sized particle impacts detected near Uranus by the Voyager 2 plasma wave instrument, *J. Geophys. Res.*, *92*, 14,959, 1987.

Gurnett, D. A., W. S. Kurth, R. L. Poynter, L. J. Granroth, I. H. Cairns, W. M. Macek, S. L. Moses, F. V. Coroniti, C. F. Kennel, and D. D. Barbosa, First plasma wave observations at Neptune, *Science*, *246*, 1494, 1989.

Hornung, K., and S. Drapatz, Residual ionization after impact of large dust particles, The Comet Halley Probe Environment, *Eur. Space Agency Spec. Publ.*, *SP-155*, 23, 1981.

Meyer-Vernet, N., M. G. Aubier, and B. M. Pedersen, Voyager 2 at Uranus: Grain impacts in the ring plane, *Geophys. Res. Lett.*, *13*, 617, 1986.

Morfill, G. E., E. Grün, and T. V. Johnson, Dust in Jupiter's magnetosphere: Physical processes, *Planet. Space Sci.*, *28*, 1087, 1980*a*.

Morfill, G. E., E. Grün, and T. V. Johnson, Dust in Jupiter's magnetosphere: Origin of the ring, *Planet. Space Sci.*, *28*, 1101, 1980*b*.

Ness, N. F., M. H. Acuña, L. F. Burlaga, J. E. P. Connerney, R. P. Lepping, and F. M. Neubauer, Magnetic fields at Neptune, *Science*, *246*, 1473, 1989.

Northrop, T. G., and J. R. Hill, The adiabatic motion of charged dust grains in rotating magnetospheres, *J. Geophys. Res.*, *88*, 1, 1983.

Scarf, F. L., and D. A. Gurnett, A plasma wave investigation for the Voyager mission, *Space Sci. Rev.*, *21*, 289, 1977.

Scarf, F. L., D. A. Gurnett, W. S. Kurth, and R. L. Poynter, Voyager 2 plasma wave observations at Saturn, *Science*, *215*, 287, 1982.

Schaffer, L., and J. A. Burns, The dynamics of weakly charged dust: Motion through Jupiter's gravitational and magnetic fields, *J. Geophys. Res.*, *92*, 2264, 1987.

Stone, E. C., and E. D. Miner, The Voyager 2 encounter with the Neptunian system, *Science*, *246*, 1417, 1989.

Warwick, J. W., D. R. Evans, J. H. Romig, J. K. Alexander, M. D. Desch, M. L. Kaiser, M. Aubier, Y. Leblanc, A. Lecacheux, and B. M. Pedersen, Planetary radio astronomy observations from Voyager 2 near Saturn, *Science*, *215*, 582, 1982.

Warwick, J. W., et al., Voyager 2 radio observations at Uranus, *Science*, *233*, 102, 1986.

Warwick, J. W., et al., Voyager planetary radio astronomy at Neptune, *Science*, *246*, 1498, 1989.

S. C. Allendorf, L. J. Granroth, D. A. Gurnett, and W. S. Kurth, Department of Physics and Astronomy, The University of Iowa, Iowa City, IA 52242.

R. L. Poynter, Jet Propulsion Laboratory, 4800 Oak Grove Drive, Pasadena, CA 91109.

(Received February 25, 1991;
revised May 2, 1991;
accepted May 3, 1991.)